The initial conditions of the point mass are given by

$$x_i = \xi, \qquad z_i = 0, \qquad \dot{x}_i = 0, \qquad \dot{z}_i = 0 \tag{27}$$

where ξ is a small perturbation in x_i. The objective is to derive the small perturbation equations of motion for the point mass using variations.

Taking the time-fixed variation of Eqs. (22) leads to

$$\tilde{\delta}\ddot{x} - 2\omega\tilde{\delta}\dot{z} - \omega^2\tilde{\delta}x + \mu[(r^3\tilde{\delta}x - x3r^2\tilde{\delta}r)/r^6] = 0$$

$$\tilde{\delta}\ddot{z} + 2\omega\tilde{\delta}\dot{x} - \omega^2\tilde{\delta}z + \mu\left\{\left[r^3\tilde{\delta}z - (z - r_0)3r^2\tilde{\delta}r\right]\Big/r^6\right\} = 0 \tag{28}$$

where

$$\tilde{\delta}r = [x\tilde{\delta}x + (z - r_0)\tilde{\delta}z]/r \tag{29}$$

Next, the coefficients of the variations are evaluated on the reference orbit ($x = z = 0$ and $r = r_0$) so that $\tilde{\delta}r = -\tilde{\delta}z$, and the CW equations become

$$\frac{\mathrm{d}^2}{\mathrm{d}t^2}\tilde{\delta}x - 2\omega\frac{\mathrm{d}}{\mathrm{d}t}\tilde{\delta}z = 0, \qquad \frac{\mathrm{d}^2}{\mathrm{d}t^2}\tilde{\delta}z + 2\omega\frac{\mathrm{d}}{\mathrm{d}t}\tilde{\delta}x - 3\omega^2\tilde{\delta}z = 0 \tag{30}$$

Finally, the initial conditions are obtained by taking the time-fixed variation of Eq. (27) and are given by

$$(\tilde{\delta}x)_i = \delta\xi, \qquad (\tilde{\delta}z)_i = 0, \qquad (\tilde{\delta}\dot{x})_i = 0, \qquad (\tilde{\delta}\dot{z})_i = 0 \tag{31}$$

If second-order terms are needed, they can be obtained by taking the variation of Eqs. (28) and (31) with $\tilde{\delta}(\delta\xi) = 0$. Once the various-order solutions have been obtained, the overall solution is given by

$$x_* = x + \tilde{\delta}x + \tfrac{1}{2!}\tilde{\delta}^2x + \cdots, \qquad z_* = z + \tilde{\delta}z + \tfrac{1}{2!}\tilde{\delta}^2z + \cdots \tag{32}$$

where x and z are zero.

Conclusions

The equations defining the various-order solutions of a problem in the realm of regular perturbation theory have been derived by using Taylor series expansions and by using variational calculus. It has been shown that the two approaches are equivalent and that the variational approach is easier to use. Variational calculus only requires differentiation, and the equations for higher-order solutions can be obtained from earlier-order equations. The same comments apply to perturbation problems involving perturbed initial conditions. Although variational calculus has only been discussed for initial-value problems, it also applies to boundary-value problems, but both time-fixed and time-free variations as well as the relationship between them are required. In fact, variational calculus applies to all problems involving neighboring curves or surfaces, for that matter.

References

[1]Hull, D. G., "On the Variational Process in Optimal Control Theory," *Journal of Optimization Theory and Applications*, Vol. 67, No. 3, 1990, pp. 447–462.

[2]Kim, T. J., and Hull, D. G., "Optimal Control Design Using Error Compensation," *Proceedings of the AIAA Guidance, Navigation, and Control Conference*, 1995, pp. 1065–1072; also *Recent Trends in Optimization Theory and Applications*, Vol. 5, World Scientific Series in Applicable Analysis, edited by R. P. Agarwal, World Scientific, NJ, 1995, pp. 41–48.

[3]Muzumdar, D. V., and Hull, D. G., "Midcourse Guidance for a Short Range Attack Missile Using Error Compensation," *Journal of Spacecraft and Rockets*, Vol. 33, No. 2, 1996, pp. 191–197.

[4]Kevorkian, J., and Cole, J. D., *Perturbation Methods in Applied Mathematics*, Vol. 34, Applied Mathematical Sciences, Springer-Verlag, New York, 1981, pp. 17–20.

[5]Ilgen, M. R., Speyer, J. L., and Leondes, C. T., "Robust Approximate Optimal Guidance Strategies for Aeroassisted Plane Change Missions: A Game Theoretic Approach," *Control and Dynamic Systems*, edited by C. T. Leondes, Vol. 52, Academic, New York, 1992, pp. 1–61.

[6]Clohessey, W. H., and Wiltshire, R. S., "Terminal Guidance Systems for Satellite Rendezvous," *Journal of the Aerospace Sciences*, Vol. 27, No. 9, 1960, pp. 653–658, 674.

[7]Roy, A. E., *Foundations of Astrodynamics*, Macmillan, New York, 1965, pp. 75, 209.

Improved Dispersion of a Fin-Stabilized Projectile Using a Passive Movable Nose

Mark Costello* and Raditya Agarwalla†
Oregon State University, Corvallis, Oregon 97331

Introduction

THE merit of a penetrator is often assessed by a relatively short list of metrics that typically includes parameters such as terminal velocity, penetrator weight, cost, system accuracy, etc. Of these parameters, system accuracy is usually near the top of the list in terms of importance and of significant concern during weapon system development. Given two identical weapon systems with the exception of accuracy, the system with superior accuracy enjoys a distinct advantage on the battlefield. A system with improved accuracy can engage targets at a greater range and obtain the same probability of hit, providing the tank commander with increased flexibility during an engagement. Alternatively, a system with better accuracy will register more first volley hits at the same range, reducing the counterfire threat. Furthermore, a gun system with superior accuracy ultimately requires fewer shots to achieve mission objectives, hence inducing less burden on the logistics pipeline.

The initial state of a projectile as it exits the gun muzzle and enters free flight can be viewed as a random process. The random nature of the initial free-flight state stems from many effects but perhaps most notably from gun tube and projectile manufacturing tolerances combined with resulting gun tube and projectile vibration. As the projectile flies downrange, these uncertainties, along with aerodynamic disturbances along the trajectory, map into dispersion at the target. A designer can take two basic approaches toward improving accuracy, that is, reduce the variability of projectile initial free-flight conditions or reduce the sensitivity of the projectile trajectory to initial free-flight conditions. One way to attack this problem using the latter approach is to replace the rigid wind screen with a passive gimballed nose. If the pivot point of the nose section is forward of the nose aerodynamic center, then the nose will tend to rotate into the relative wind and subsequently reduce aerodynamic jump caused by projectile normal force. A passive gimballed nose projectile is an attractive design modification because it is a relatively simple mechanism that requires no active electronic controls. Furthermore, for many penetrator designs, the nose cone is empty and could easily house the gimbal joint.

Early in the development of controlled rockets, the notion of utilizing a movable nose to control the trajectory of a projectile actively was established.[1] Goddard obtained a patent that outlined the basic concept. More recently, Barrett and Stutts[2] further developed this concept. The movable nose concept has also been investigated in unguided projectile applications as well. Kranz[3] obtained a patent for a telescopic gimballed nose on a high-velocity aerodynamic body. Schmidt and Donovan[4] developed a simple closed-form solution for an effective $C_{L\alpha}$ and $C_{M\alpha}$ for a movable nose projectile configuration that is based on projectile linear theory.[5] A limited number of prototype projectiles were fired, and range data were reduced to estimate aerodynamic coefficients. The work reported here extends the previous work mentioned by simulating the exterior ballistics of a gimballed nose projectile in atmospheric flight and subsequently comparing impact point dispersion statistics with a similarly sized rigid projectile.

Received 10 April 2000; revision received 10 May 2000; accepted for publication 10 May 2000.

*Assistant Professor, Department of Mechanical Engineering. Member AIAA.

†Graduate Research Assistant, Department of Mechanical Engineering.

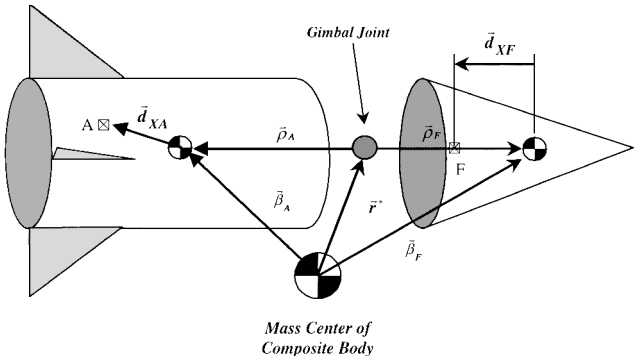

Fig. 1 Schematic of the gimballed nose projectile configuration.

Gimbal Nose Projectile Dynamic Model

A schematic of the gimballed nose projectile configuration is shown in Fig. 1. The gimballed nose projectile consists of forward and aft projectile sections. The configuration possesses three position degrees of freedom, which are the inertial position components of the mass center of the composite body described in an inertial reference frame. A total of six degrees of freedom describe the aft and forward body orientation. The orientation of the aft projectile is obtained through a sequence of three body-fixed rotations. Starting from an inertial coordinate system, the aft body is successively rotated through Euler yaw, pitch, and roll angles to arrive at its final orientation in space. The forward body orientation is also obtained by a sequence of three body-fixed rotations. Starting from the aft body reference frame, the forward body is successively rotated through Euler yaw, pitch, and roll angles to arrive at its final orientation in space. With these definitions, a rigid projectile configuration is realized when the forward body Euler angles are zero, $\phi_F = \theta_F = \psi_F = 0$. The velocity vector components of the mass center of the composite body are defined in the aft body reference frame, and the resulting translational kinematic differential equations are given by

$$\begin{Bmatrix} \dot{x} \\ \dot{y} \\ \dot{z} \end{Bmatrix} = [T_A] \begin{Bmatrix} u \\ v \\ w \end{Bmatrix} \tag{1}$$

Equation (1) contains the transformation matrix from the aft body reference frame to the inertial reference frame, T_A. The transformation from the forward body reference frame to the aft body reference frame is T_F.

The angular velocity vector expressions for the aft and forward bodies, respectively, with respect to an inertial reference frame are

$$\boldsymbol{\omega}_{A/I} = p_A \boldsymbol{i}_A + q_A j_A + r_A \boldsymbol{k}_A \tag{2}$$

$$\boldsymbol{\omega}_{F/I} = p_F \boldsymbol{i}_F + q_F j_F + r_F \boldsymbol{k}_F \tag{3}$$

With these definitions, the rotational kinematic differential equations are given by

$$\begin{Bmatrix} \dot{\phi}_A \\ \dot{\theta}_A \\ \dot{\psi}_A \end{Bmatrix} = \begin{bmatrix} 1 & s_{\phi_A} t_{\theta_A} & c_{\phi_A} t_{\theta_A} \\ 0 & c_{\phi_A} & -s_{\phi_A} \\ 0 & s_{\phi_A}/c_{\theta_A} & c_{\phi_A}/c_{\theta_A} \end{bmatrix} \begin{Bmatrix} p_A \\ q_A \\ r_A \end{Bmatrix} \tag{4}$$

$$\begin{Bmatrix} \dot{\phi}_F \\ \dot{\theta}_F \\ \dot{\psi}_F \end{Bmatrix} = \begin{bmatrix} 1 & s_{\phi_F} t_{\theta_F} & c_{\phi_F} t_{\theta_F} \\ 0 & c_{\phi_F} & -s_{\phi_F} \\ 0 & s_{\phi_F}/c_{\theta_F} & c_{\phi_F}/c_{\theta_F} \end{bmatrix} \left(\begin{Bmatrix} p_F \\ q_F \\ r_F \end{Bmatrix} - T_F{}^T \begin{Bmatrix} p_A \\ q_A \\ r_A \end{Bmatrix} \right) \tag{5}$$

The translation dynamic equations for the mass center of the composite body are given by

$$\begin{Bmatrix} \dot{u} \\ \dot{v} \\ \dot{w} \end{Bmatrix} = \begin{bmatrix} 0 & r_A & -q_A \\ -r_A & 0 & p_A \\ q_A & -p_A & 0 \end{bmatrix} \begin{Bmatrix} u \\ v \\ w \end{Bmatrix} + \frac{1}{m_A + m_F} \begin{Bmatrix} X \\ Y \\ Z \end{Bmatrix} \tag{6}$$

In Eq. (6), the first term on the right-hand side utilizes the aft body angular velocity components in the cross product operator because the composite body mass center velocity components are defined in the aft body reference frame. The total applied force vector components are given in the aft body reference frame.

The rotational dynamics of the forward and aft projectile sections are derived by first splitting the system at the gimbal joint, which exposes the constraint forces and moments at the joint. As shown in Eq. (7), by subtracting the force balance of both bodies, the components of the constraint force in the aft body coordinate system can be written in terms of the rotational state variables and their derivatives:

$$\begin{Bmatrix} X_C \\ Y_C \\ Z_C \end{Bmatrix} = A_A \begin{Bmatrix} \dot{p}_A \\ \dot{q}_A \\ \dot{r}_A \end{Bmatrix} + A_F \begin{Bmatrix} \dot{p}_F \\ \dot{q}_F \\ \dot{r}_F \end{Bmatrix} + \{B_{AF}\} \tag{7}$$

where

$$A_A = [m_A m_F/(m_A + m_F)] S_{\rho_A} \tag{8}$$

$$A_F = [m_A m_F/(m_A + m_F)] T_F S_{\rho_F} \tag{9}$$

$$B_{AF} = \frac{m_F}{m_A + m_F} \begin{Bmatrix} X_A \\ Y_A \\ Z_A \end{Bmatrix} - \frac{m_A}{m_A + m_F} T_F \begin{Bmatrix} X_F \\ Y_F \\ Z_F \end{Bmatrix} + \frac{m_A m_F}{m_A + m_F} S_{\omega_A} S_{\omega_A} \begin{Bmatrix} \rho_{A_X} \\ \rho_{A_Y} \\ \rho_{A_Z} \end{Bmatrix} - T_F S_{\omega_F} S_{\omega_F} \begin{Bmatrix} \rho_{F_X} \\ \rho_{F_Y} \\ \rho_{F_Z} \end{Bmatrix} \tag{10}$$

where $S_{(\cdot)}$ denotes the cross product operator.[6]

The constraint moment at the gimbal joint is generated by friction in the joint and potentially by geometric interference between the nose and main projectile body when the total angle between the nose and projectile axes of symmetry exceeds a specific value. Gimbal joint friction is modeled as viscous damping. The gimbal joint friction constraint moment is proportional to the difference in angular velocity between the two projectile body components. Geometric interference is modeled as a stiff linear torsion spring with dead band. The dead band region corresponds to the rotational envelope of the nose with respect to the main projectile body. The gimbal nose geometric interference constraint moment magnitude is proportional to the angle between $\boldsymbol{i}_A$ and $\boldsymbol{i}_F$, denoted α_g, and is computed using

$$\alpha_g = \cos^{-1}(\cos\theta_F \cos\psi_F) \tag{11}$$

The direction of this moment is perpendicular to the plane formed by $\boldsymbol{i}_A$ and $\boldsymbol{i}_F$. Equation (12) provides an expression for the gimbal joint constraint moment:

$$\begin{Bmatrix} L_C \\ M_C \\ N_C \end{Bmatrix} = K_g \frac{M_g}{\sqrt{\sin^2(\theta_F) + \cos^2(\theta_F)\sin^2(\psi_F)}} \times \begin{Bmatrix} 0 \\ -\sin(\theta_F) \\ -\cos(\theta_F)\sin(\psi_F) \end{Bmatrix} + C_g \begin{Bmatrix} \delta p \\ \delta q \\ \delta r \end{Bmatrix} \tag{12}$$

where

$$M_g = \begin{cases} 0 & \alpha_g \le \alpha^* \\ K_g(\alpha_g - \alpha^*) & \alpha_g > \alpha^* \end{cases} \tag{13}$$

$$\begin{Bmatrix} \delta p \\ \delta q \\ \delta r \end{Bmatrix} = \begin{Bmatrix} p_A \\ q_A \\ r_A \end{Bmatrix} - [T_F] \begin{Bmatrix} p_F \\ q_F \\ r_F \end{Bmatrix} \tag{14}$$

The first term in Eq. (12) is the geometric interference constraint moment whereas the second term represents the friction constraint moment. Notice that when $\boldsymbol{i}_A$ and $\boldsymbol{i}_F$ are aligned ($\alpha_g = 0$), the interference constraint moment is singular. Fortunately, this singularity is avoided because the gimbal joint interference constraint moment is zero in this case.

The rotational dynamic equations of the aft and forward projectile bodies, respectively, are given by

$$I_A \begin{Bmatrix} \dot{p}_A \\ \dot{q}_A \\ \dot{r}_A \end{Bmatrix} + S_{\omega_A} I_A \begin{Bmatrix} p_A \\ q_A \\ r_A \end{Bmatrix} = -\begin{Bmatrix} L_C \\ M_C \\ N_C \end{Bmatrix} + \begin{Bmatrix} L_A \\ M_A \\ N_A \end{Bmatrix} + S_{\rho_A} \begin{Bmatrix} X_C \\ Y_C \\ Z_C \end{Bmatrix} \tag{15}$$

$$T_F I_F \begin{Bmatrix} \dot{p}_F \\ \dot{q}_F \\ \dot{r}_F \end{Bmatrix} + T_F S_{\omega_F} I_F \begin{Bmatrix} p_F \\ q_F \\ r_F \end{Bmatrix} = \begin{Bmatrix} L_C \\ M_C \\ N_C \end{Bmatrix} + T_F \begin{Bmatrix} L_F \\ M_F \\ N_F \end{Bmatrix} - T_F S_{\tilde{\rho}_F} \begin{Bmatrix} X_C \\ Y_C \\ Z_C \end{Bmatrix} \tag{16}$$

By the substituting of the constraint force and moment expressions into Eqs. (15) and (16), the final form of the rotational dynamic equations is obtained and expressed as

$$\begin{bmatrix} I_A - S_{\rho_A} A_A & -S_{\rho_A} A_F \\ T_F S_{\tilde{\rho}_F} A_A & T_F I_F + T_F S_{\tilde{\rho}_F} A_F \end{bmatrix} \begin{Bmatrix} \dot{p}_A \\ \dot{q}_A \\ \dot{r}_A \\ \dot{p}_F \\ \dot{q}_F \\ \dot{r}_F \end{Bmatrix} = \begin{Bmatrix} g_{A_X} \\ g_{A_Y} \\ g_{A_Z} \\ g_{F_X} \\ g_{F_Y} \\ g_{F_Z} \end{Bmatrix} \tag{17}$$

where

$$\{g_A\} = -S_{\omega_A} I_A \begin{Bmatrix} p_A \\ q_A \\ r_A \end{Bmatrix} - \begin{Bmatrix} L_C \\ M_C \\ N_C \end{Bmatrix} + \begin{Bmatrix} L_A \\ M_A \\ N_A \end{Bmatrix} + S_{\rho_A} \{B_{AF}\} \tag{18}$$

$$\{g_F\} = -T_F S_{\omega_F} I_F \begin{Bmatrix} p_F \\ q_F \\ r_F \end{Bmatrix} + \begin{Bmatrix} L_C \\ M_C \\ N_C \end{Bmatrix} + T_F \begin{Bmatrix} L_F \\ M_F \\ N_F \end{Bmatrix} - T_F S_{\tilde{\rho}_F} \{B_{AF}\} \tag{19}$$

Collectively, Eqs. (1), (4–6), and (17) constitute the gimbal nose projectile dynamic model.

The total external load acting on the composite body is due to weight and steady aerodynamic forces on both the forward and aft body projectile components. The weight force components in the aft body reference frame is given by

$$\begin{Bmatrix} X_G \\ Y_G \\ Z_G \end{Bmatrix} = (m_A + m_F) g \begin{Bmatrix} -s_{\theta_A} \\ c_{\theta_A} s_{\phi_A} \\ c_{\theta_A} c_{\phi_A} \end{Bmatrix} \tag{20}$$

The steady aerodynamic force on the aft body is provided by

$$\begin{Bmatrix} X_A \\ Y_A \\ Z_A \end{Bmatrix} = -\frac{1}{2}\rho \left(\frac{\pi D^2}{4}\right) \times \begin{Bmatrix} \left(C^A_{X0} + C^A_{X2} \dfrac{v^2 + w^2}{\sqrt{u^2 + v^2 + w^2}}\right)(u^2 + v^2 + w^2) \\ C^A_{N_\alpha} v \sqrt{u^2 + v^2 + w^2} \\ C^A_{N_\alpha} w \sqrt{u^2 + v^2 + w^2} \end{Bmatrix} \tag{21}$$

Expressions for the forward body aerodynamic forces take on the same form as Eq. (21). Aerodynamic coefficients in Eq. (21) depend on local Mach number at the projectile mass center and are computed using linear interpolation from tabulated data. The right-hand-side terms in Eq. (17) contain the external moments acting on each section of the projectile. These equations contain contributions from steady and unsteady aerodynamics. The steady aerodynamic moments are computed for each individual body with a cross product between the steady body aerodynamic force vector and the distance vector from the center of gravity to the center of pressure. The unsteady body aerodynamic moments provide a damping source for projectile angular motion and are given for the forward body by

$$\begin{Bmatrix} L^F_{UA} \\ M^F_{UA} \\ N^F_{UA} \end{Bmatrix} = \tilde{q}_a D \begin{Bmatrix} C^F_{DD} + \dfrac{p_F D C^F_{LP}}{2V} \\ \dfrac{q_F D C^F_{MQ}}{2V} \\ \dfrac{r_F D C^F_{NR}}{2V} \end{Bmatrix} \tag{22}$$

where

$$\tilde{q}_a = \tfrac{1}{8}\rho(u^2 + v^2 + w^2)\,\pi D^2 \tag{23}$$

The expression for the aft section takes on similar form. Air density is computed using the center of gravity position of the projectile in concert with the standard atmosphere. Finally, the total aerodynamic angle of attack of the aft section is defined,

$$\alpha_A = \tan^{-1}\left(\sqrt{v^2 + w^2}\big/u\right) \tag{24}$$

The aerodynamic angle of attack of the forward body is computed in the same manner except the velocity components are first converted to the forward body reference frame.

Results

The equations of motion for the nine-degree-of-freedom gimbal nose projectile model discussed and a six-degree-of-freedom rigid projectile model[7] were numerically integrated to obtain simulated impact points at 1 and 3 km. The simulation results that follow use a generic 120-mm-long rod penetrator with a mass of 3.2 kg. The muzzle velocity of the projectile is 1700 m/s launched at a quadrant elevation angle of 5 deg. The equations of motion were integrated using a fourth-order Runge–Kutta scheme with a time step of 0.000001 s.

Dispersion at the target was created through Monte Carlo simulation of the initial pitch and yaw rate of the projectile. The initial pitch and yaw rates were modeled as independent Gaussian random

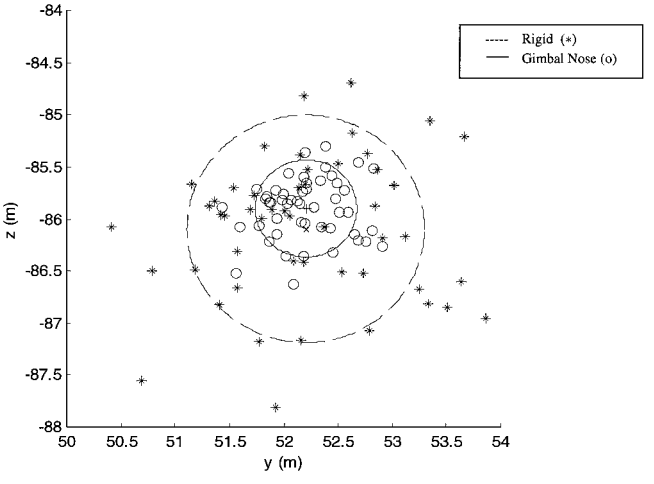

Fig. 2 Impact point dispersion at 1-km range.

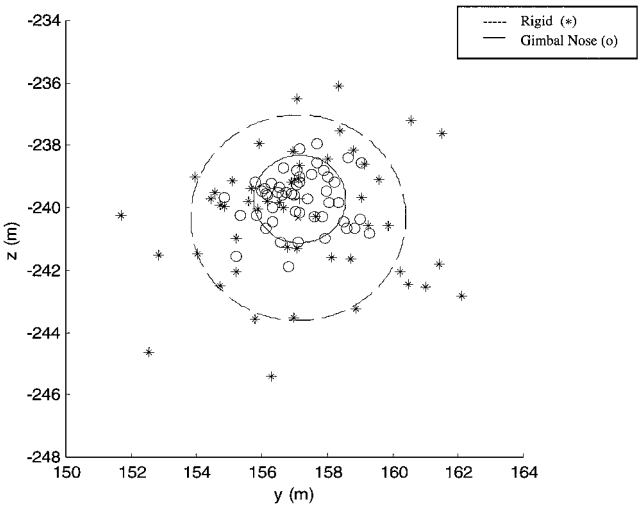

Fig. 3 Impact point dispersion at 3-km range.

variables with a mean of zero and standard deviation of 3 rad/s. A sample size of 50 simulations was used in computing impact point dispersion statistics. Figures 2 and 3 show the Monte Carlo simulation impact points for the baseline rigid and gimbal nose projectile configurations at a range of 1 and 3 km, respectively. In both charts, the circles correspond to a region such that 66% of the shot impacts fall within the circle. The large dashed circle corresponds to the rigid projectile whereas the small solid circle corresponds to the gimbal nose configuration. The dispersion circle radii for the rigid projectile at 1 and 3 km is 1.1 and 3.3 m whereas the dispersion circle radii for the gimbal nose projectile at 1 and 3 km is 0.5 and 1.4 m, respectively. Notice that the mean impact point of the two projectile configurations is different. The ratio of the dispersion circle radius for the gimbal nose to rigid projectile configuration is 0.43 and is independent of range. Thus, for the example penetrator projectile equipped with a gimbal nose, dispersion at any range can be reduced by a factor of 0.43.

Conclusions

A penetrator projectile equipped with a gimbal nose wind screen has the potential to reduce impact point dispersion drastically. By the mounting of the gimbal joint forward of the nose aerodynamic center, the nose tends to turn into the wind and reduces the sensitivity of the trajectory to launch disturbances. In the example case considered, impact point dispersion was reduced by more than 50%. The mean impact point of the rigid and gimbal nose projectile configurations are different, which will require fire control system logic to be modified depending on the particular projectile configuration being launched.

References

[1]Goddard, R. H., "Apparatus for Steering Aircraft," U.S. Patent 2594766, April 1952.

[2]Barrett, R., and Stutts, J., "Modeling, Design, and Testing of a Barrel-Launched Adaptive Munition," *Proceedings of the 4th Annual Society of Photo-Optical Engineers Symposium on Smart Structures*, Society of Photo-Optical Engineers, New York, 1997.

[3]Kranz, W., "High Velocity Aerodynamic Body Having Telescopic Nose Tip," U.S. Patent 4756492, July 1988.

[4]Schmidt, E., and Donovan, W., "Technique to Reduce Yaw and Jump of Fin-Stabilized Projectiles," *Journal of Spacecraft and Rockets*, Vol. 35, No. 1, 1998, pp. 110, 111.

[5]Murphy, C., "Free Flight Motion of Symmetric Missiles," U.S. Army Ballistic Research Lab., BRL Rept. 1216, Aberdeen Proving Ground, MD, July 1963.

[6]Angeles, J., *Fundamentals of Robotic Mechanical Systems*, Springer-Verlag, New York, 1997, pp. 28–30.

[7]Costello, M. F., and Anderson, D. P., "Effect of Internal Mass Unbalance on the Terminal Accuracy and Stability of a Field Artillery Projectile," *Proceedings of the 1996 AIAA Atmospheric Flight Mechanics Conference*, AIAA, Reston, VA, 1996.

Multi-Input, Multi-Output, Band-Limited Transducer Selection for Disturbance Rejection

Robert L. Clark*
Duke University, Durham, North Carolina 27708-0300
and
David E. Cox†
NASA Langley Research Center, Hampton, Virginia 23681-0001

Introduction

A BAND-LIMITED actuator/sensor selection methodology for disturbance rejection was previously developed.[1] Unlike prior methods, which emphasized disturbance rejection in selecting transducers that couple best to modes present in the performance path,[2–6] the methodology proposed by Clark and Cox[1] serves to further impose a penalty on the selection of transducer pairs that couple well to modes beyond the identified bandwidth of interest, creating a "natural" roll off in the frequency response from the selected spatial apertures of the transducers. In a more recent publication Smith and Clark[4] proposed a modification to the performance metric identified by Clark and Cox, providing a mechanism for selectively identifying modes to be controlled and modes to be ignored. Transducer pairs are chosen from a predetermined set based upon their selective coupling to identified modes for performance and lack of coupling to all other modes included in the model.

All of these design approaches are derived from the original work used in selecting actuator and sensor locations from a predetermined set of candidate locations based upon the Hankel singular values of the controllability and observability Gramians of flexible structures.[7,8] Within the original formulation, the actuator/sensor selection methodology was based entirely upon the Hankel singular values of the control path P_{yu} for some finite set of modes and some predetermined set of actuators and sensors.[7,8] Later revisions to this method have included a weighting of the Hankel singular values of the control path P_{yu} by that of the Hankel singular values of the performance path P_{zw} (Refs. 2 and 3). In the most recent extensions the actuator/sensor selection methodology based upon the disturbance rejection approach was modified with an additional metric aimed at robustness with respect to modes not targeted in the performance metric.[1,4]

A method of rank-ordering transducer pairs for control results from all of the design approaches is described.[1–8] Although the performance metrics allow the designer to select the best single-input, single-output (SISO) transducer pair from the predetermined target set, if more than one transducer pair is desired a multi-input, multi-output (MIMO) metric must be applied. The purpose of this Note is to introduce the MIMO design procedure and distinguish it from the SISO design approach. As will be demonstrated by example, one cannot simply select the rank-ordered SISO transducer pairs for the MIMO application when both in-bandwidth coupling and out-of-bandwidth roll off are part of the performance metric.

MIMO Band-Limited Placement Metric for Disturbance Rejection

For convenience the design problem can be cast in the standard two-port model as shown in Fig. 1. The upper transfer matrix $P_{zw}(s)$ represents the path from disturbances $w(s)$ to a measure of the system performance $z(s)$. This path is determined by the definition of

Received 27 December 1999; revision received 5 June 2000; accepted for publication 8 June 2000.

*Professor, Department of Mechanical Engineering and Materials Science, Box 90300. Member AIAA.

†Research Scientist.